J. Fluid Mech. (2014), vol. 749, pp. 297–319. © Cambridge University Press 2014
doi:10.1017/jfm.2014.237

# On calculating forces from the flow field with application to experimental volume data

**Adam C. DeVoria**‡, **Zakery R. Carr**§ **and Matthew J. Ringuette**†

Department of Mechanical and Aerospace Engineering, State University of New York, Buffalo, NY 14260, USA

(Received 24 November 2013; revised 4 February 2014; accepted 24 April 2014; first published online 15 May 2014)

The use of flow field information to compute the fluid dynamic force on a body is investigated with specific application to experimental volumetric measurements. The calculation method used avoids the explicit evaluation of the pressure on the boundaries. It is shown that errors in the data introduce an artificial dependence of the calculations on the position origin, and also that these errors are amplified by the position vector. A statistical description of the calculation variation associated with origin dependence is presented. A method is developed that objectively determines an origin which reduces the effect of the amplified error. The method utilises mathematical identities which relate the measurements to the main sources of error in a physically meaningful way, and is also found to be effective for changes of the external and internal boundaries of the fluid.

**Key words:** biological fluid dynamics, mathematical foundations, vortex flows

## 1. Introduction

The calculation of fluid dynamic forces on moving bodies from flow field information is important for a great number of applications. There are numerous methods available, and the success of any particular one is related to the type of problem being analysed. For analytical problems, the integral form of the momentum equation usually succeeds only for steady flows (Batchelor 1967), since then a detailed knowledge of the entire velocity field is not required. For unsteady problems with externally unbounded fluid, this approach is partly redeemed using asymptotic limits. However, defining total fluid momentum in an infinite region is not without difficulty (see e.g. Lighthill 1986) and commonly the concept of the distributed hydrodynamic impulse is introduced, which has an integrated value consistent with the total momentum. Although computation of the hydrodynamic impulse requires knowledge of the vorticity field (in place of the velocity), this approach has utility for analytical work as many flows are more easily described and understood through the vorticity.

Use of the hydrodynamic impulse to determine forces is common in numerical approaches. However, many simulations also typically resolve large velocity gradients

† Email address for correspondence: ringum@buffalo.edu
‡ Present address: University of Florida, Gainesville, FL 32611, USA.
§ Present address: CUBRC Inc., Buffalo, NY 14225, USA.

near bodies, and so the total stress on the body may be accurately obtained and integrated to yield the resultant force. Conversely, in most experiments, resolving boundary layers near surfaces is not feasible. Forces may be directly measurable, but this can be difficult for low Reynolds number (*Re*) flows. Using velocity fields measured with digital particle image velocimetry (DPIV), several researchers have successfully calculated forces on bodies via standard control volume (CV) methods (e.g. Unal, Lin & Rockwell 1997; Kurtulus, Scarano & David 2007; van Oudheusden *et al.* 2007; David, Jardin & Farcy 2009; Jardin, David & Farcy 2009; Spedding & Hedenstrom 2009; Sällström & Ukeiley 2014; Villegas & Diez 2014). In this approach the pressure on the control surface is typically obtained by spatial integration of the pressure gradient in the equations of motion; this and other image-based pressure methods are discussed in van Oudheusden (2013). Others have used equations involving the hydrodynamic impulse to calculate forces (e.g. Lin & Rockwell 1996; Noca, Shiels & Jeon 1999; DeVoria & Ringuette 2013).

David *et al.* (2009) performed simulations and planar DPIV experiments for a translating NACA0012 airfoil section at 45° angle of attack and $Re = 1000$. Using the simulations to compute forces from a CV approach, they investigated several practical effects, such as spatial and temporal resolutions and the addition of random noise to the numerical data. They found that velocity noise most significantly affects the pressure term when flow structures cross the bounding outer surfaces. Using the same CV method, the experimentally determined forces exhibit appreciable discrepancies with the computations, which were attributed to experimental errors degrading the pressure calculation. However, these forces were observed to have a spatiotemporal correlation with the vortex dynamics in the wake flow, implying a qualitative validation.

The majority of experimental work aiming to determine fluid dynamic forces from the flow field has been applied to two-dimensional flows. However, Poelma, Dickson & Dickinson (2006) measured the three-dimensional velocity field around a scaled fruit fly wing model using stereoscopic DPIV (S-DPIV) volume reconstructions. They calculated the force on the wing from the equation developed by Wu (1981) and achieved reasonable results despite the fact that external control surface terms are not accounted for in the equation, as it is technically valid only for an infinite fluid. Poelma *et al.* (2006) comment on this and also on the fact that portions of the wing and the vorticity field are not contained in their measurement volume. Rangi, van Oudheusden & Scarano (2011) used a similar method to measure the transonic flow within a thin volumetric slab near the blade tip of an aircraft propeller. They computed the pressure field around and on the blade section, as well as the spanwise force distribution along the span of the blade section. Both quantities compared favourably with those determined from simulation data. Tronchin, David & Farcy (2013) used the high-speed laser-scanning tomographic DPIV method developed by David *et al.* (2012) to measure the flow around a flapping NACA0012 airfoil at $Re = 1000$. They computed forces from a CV approach and from integrating the stress on the surface of the foil. Both methods yielded similar results and compared reasonably well with numerical data.

The lack of volumetric S-DPIV data for three-dimensional flows stems from the time-consuming and intensive techniques required to obtain them (see Poelma *et al.* 2006; Lu & Shen 2008; Ozen & Rockwell 2012; Carr, Chen & Ringuette 2013). However, with the increasing use of volumetric velocimetry techniques, there is a need to investigate the practical aspects of using these experimental data to predict fluid dynamic forces. This is the aim of the current paper and is assessed by investigating aspects such as artificial origin and boundary dependence. The three-dimensional velocity data of Carr *et al.* (2013) for the flow around rotating plates are employed as test cases. First, a brief discussion is given in § 2 on the different theoretical concepts and equations used, the main purpose being to provide clarity to the equivalence among them. Section 3 presents some of the practical issues that arise when experimental data are used to calculate forces. An overview of the details of the experimental set-up of Carr *et al.* (2013) is given in § 4. Section 5.1 describes how errors in the data are amplified by the position vector and lead to an artificial dependence of the calculation on the location of the coordinate origin. A method to reduce these errors is also introduced. A similar artificial dependence on the boundaries of the CV is addressed in § 5.2. Lastly, force calculations from the flow data are presented in § 5.3 and are compared with direct measurements.

## 2. Theoretical considerations

In analysing the fluid dynamic force on a moving body, $\boldsymbol{F}(t)$, several approaches may be used to represent certain contributions and these are distinguished primarily by how the internal boundary of the fluid is treated. Noca *et al.* (1999) defined a volume containing only fluid, which is externally bounded, as well as internally bounded by a surface coincident with the body. They derived various equations that eliminate the pressure and are general in that the volume is finite and non-material, the latter allowing for relative motion of the external boundary as well as porosity through the body. A useful vector/integral identity employed by both Saffman (1992) and Noca *et al.* (1999) that expands the volume integral of a vector field, $\boldsymbol{a}$, is given by

$$\int_V \boldsymbol{x} \times (\boldsymbol{\nabla} \times \boldsymbol{a}) \mathrm{d}V = (N-1) \int_V \boldsymbol{a} \mathrm{d}V + \oint_S \boldsymbol{x} \times (\hat{\boldsymbol{n}} \times \boldsymbol{a}) \mathrm{d}S, \tag{2.1}$$

where $N = \boldsymbol{\nabla} \cdot \boldsymbol{x}$ is the dimension of space and $V$ is a volume bounded by a surface $S$ with *outward* normal $\hat{\boldsymbol{n}}$.

We start with the integral momentum equation for an incompressible fluid enclosing a solid body, and expand the volume integral of momentum using (2.1). The fluid volume is $V_f$ and is bounded internally by $S_b$ and externally by $S_e$, so that $S = S_b \cup S_e$ (see figure 1), and so

$$\begin{aligned} \boldsymbol{F}(t) = {} & \frac{1}{N-1} \rho \frac{\mathrm{d}}{\mathrm{d}t} \left[ -\int_{V_f} \boldsymbol{x} \times \boldsymbol{\omega} \mathrm{d}V + \oint_{S_b} \boldsymbol{x} \times (\hat{\boldsymbol{n}} \times \boldsymbol{u}) \mathrm{d}S + \oint_{S_e} \boldsymbol{x} \times (\hat{\boldsymbol{n}} \times \boldsymbol{u}) \mathrm{d}S \right] \\ & + \oint_{S_e} \hat{\boldsymbol{n}} \cdot \left[ -p\boldsymbol{I} - (\boldsymbol{u} - \boldsymbol{u}_e) \otimes \boldsymbol{u} + \boldsymbol{T} \right] \mathrm{d}S, \end{aligned} \tag{2.2}$$

where $\rho$ is the fluid density, $\boldsymbol{u}_e$ the velocity of the external boundary, $p$ the pressure, $\boldsymbol{I}$ the identity tensor and $\boldsymbol{T}$ the deviatoric stress tensor. It can be shown that the *total* integral over $S_e$ vanishes upon letting $S_e$ approach infinity, giving the classical result for an externally unbounded fluid. Specifically, the viscous and convective flux terms tend to zero, whereas the contribution from the pressure term is non-vanishing, but cancels with that of the third term (including the time derivative) in (2.2).

Alternatively, the body may be replaced with fluid (i.e. fluidic body), which allows integration through the body (e.g. Saffman 1992). The integral over $S_b$ may then be

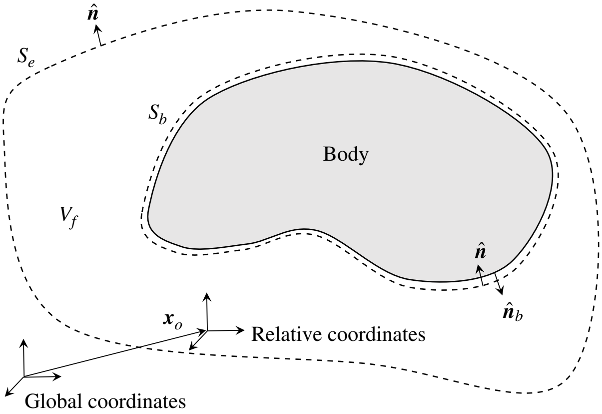

FIGURE 1. Definition of the CV. The fluid volume is $V_f$ and is bounded by the external, $S_e$, and internal, $S_b$, boundaries. Here $S_b$ coincides with the body surface. The outward normal of the control surface is $\hat{\boldsymbol{n}}$ and that of the body is $\hat{\boldsymbol{n}}_b$. Also shown is a global coordinate system and the vector $\boldsymbol{x}_o$ that defines the arbitrary origin of a relative coordinate system.

transformed by use of (2.1). If $\hat{\boldsymbol{n}}_b$ is the outward normal of the surface of the body that coincides with $S_b$, then $\hat{\boldsymbol{n}}_b = -\hat{\boldsymbol{n}}$ and we obtain from (2.2)

$$\begin{aligned}\boldsymbol{F}(t) = {} & \frac{1}{N-1}\rho\frac{\mathrm{d}}{\mathrm{d}t}\left[-\int_V \boldsymbol{x}\times\boldsymbol{\omega}\,\mathrm{d}V + \oint_{S_e}\boldsymbol{x}\times(\hat{\boldsymbol{n}}\times\boldsymbol{u})\,\mathrm{d}S\right] + \rho\frac{\mathrm{d}}{\mathrm{d}t}\int_{V_b}\boldsymbol{u}\,\mathrm{d}V \\ & + \oint_{S_e}\hat{\boldsymbol{n}}\boldsymbol{\cdot}[-p\boldsymbol{I} - (\boldsymbol{u}-\boldsymbol{u}_e)\otimes\boldsymbol{u} + \boldsymbol{T}]\,\mathrm{d}S, \end{aligned} \tag{2.3}$$

where $V_b$ is the volume of the body and $V = V_f \cup V_b$, the integral over which includes the vorticity in the body. Equation (2.3) is valid for a bounded fluid, and is a generalisation of the results given by Wu (1981) since, as with (2.2), the total integral over $S_e$ vanishes when the fluid becomes infinite. Wu (1981) maintains solid bodies, but essentially employs the fluidic body concept in his final result. The term with integration over $V_b$ is the inertia force of the *fluidic* body and for this reason it is sometimes confused with the added mass force; equation (2.3) is the total force and need not make explicit distinctions among contributions, as was stated by Poelma *et al.* (2006) in reference to the asymptotic equation.

However, to this end we can obtain the potential force contribution by transforming the integral over $S_b$ in (2.2) in a different manner. Following Saffman (1992, p. 77) and using (2.1) it can be shown that

$$\rho\oint_{S_b}\boldsymbol{x}\times(\hat{\boldsymbol{n}}\times\boldsymbol{u})\,\mathrm{d}S = -(N-1)\rho\oint_{S_b}\phi\hat{\boldsymbol{n}}\,\mathrm{d}S, \tag{2.4}$$

where $(-\rho\phi)$ is often called the ‘pressure–impulse’ associated with the potential, $\phi$. Then (2.4) may be rewritten in terms of inertia coefficients, or added/virtual masses; Howe (2007) gives formulae for contributions due to both translation and rotation of the body. Although the potential is an irrotational flow concept, it is applicable in a viscous fluid when considered to be established by an incremental change of the body velocity (see Appendix of Leonard & Roshko 2001). This is consistent with Lighthill's concept of dividing up the flow into a potential flow (vortex sheet coincident with the body) and a vortex flow (the remaining 'additional vorticity'), each of which result in a distinct force contribution (Lighthill 1986; Williamson & Govardhan 2004). Lighthill (1986) considered an externally unbounded fluid, but inspection of (2.2) shows that these contributions are given by the first two terms, upon using (2.4). The remaining terms again represent the finite control surface contributions, which vanish for an infinite fluid region.

## 3. Practical considerations

Here, we form an equation that caters to features typical of experimental velocity data obtained by S-DPIV. We choose to avoid directly evaluating the pressure on $S_e$, because of the errors inherent to DPIV measurements, which are known to exacerbate propagation errors in the pressure calculation (Kurtulus *et al.* 2007; David *et al.* 2009; van Oudheusden 2013) and, furthermore, no initial condition is required. Following the manipulations of Noca *et al.* (1999) to remove the pressure from (2.2), one can show that

$$\boldsymbol{F}(t) = -\rho \frac{\mathrm{d}}{\mathrm{d}t}\int_{V_f} \boldsymbol{u}\,\mathrm{d}V - \frac{1}{N-1}\rho\frac{\mathrm{d}}{\mathrm{d}t}\oint_{S_e} \boldsymbol{x}\times(\hat{\boldsymbol{n}}\times\boldsymbol{u})\,\mathrm{d}S + \oint_{S_e}\hat{\boldsymbol{n}}\boldsymbol{\cdot}\boldsymbol{B}\,\mathrm{d}S, \tag{3.1}$$

where

$$\boldsymbol{B}(\boldsymbol{x},t) = \boldsymbol{T} - \rho\boldsymbol{u}\otimes\boldsymbol{u} + \frac{\hat{\boldsymbol{n}}\otimes\boldsymbol{x}\times\hat{\boldsymbol{n}}\times(\nabla\boldsymbol{\cdot}\boldsymbol{T} - \rho\boldsymbol{u}\boldsymbol{\cdot}\nabla\boldsymbol{u}) + \rho\boldsymbol{u}_e\otimes\boldsymbol{x}\times\boldsymbol{\omega}}{N-1}. \tag{3.2}$$

Although the elimination of the pressure essentially substitutes in spatial derivatives, which are affected by the spatial resolution of the data, the relation is exact. Note that Noca *et al.* (1999) perform several further vector manipulations to the terms cross-multiplying $\boldsymbol{x}$ in (3.2).

Obtaining S-DPIV volume reconstructions presents a balance between temporal resolution and realistic overall measurement acquisition time. Namely, spatial resolution and samples for phase-averaging may be favoured over temporal resolution, leading to larger temporal discretisation error. For example, the test cases studied here required approximately 4–6 days of completely automated data acquisition to achieve the desired spanwise spatial and angular resolutions, with an additional 1–2 days of DPIV processing. An alternative that somewhat alleviates this experimental effort is the high-speed laser scanning tomographic DPIV method developed by David *et al.* (2012). The data acquisition involves an oscillating mirror which scans the laser plane along the entire measurement volume in a short time. If the flow time scales are much larger than the scanning time, then the volumetric measurement acquisition may be considered instantaneous. However, to obtain the time-dependent flow the same phase-locking method used in S-DPIV reconstructions must be employed, and likewise for phase-averaging.

Unal *et al.* (1997) discuss the effect of temporal resolution of DPIV data on force calculation using a CV method. They state that the time derivative of the integral of momentum is most affected. Alternatively, Lin & Rockwell (1996) used the hydrodynamic impulse concept and fit a polynomial to the resulting force impulse data *prior* to taking time derivatives. This bypasses a numerical derivative of the momentum integral, but the temporal resolution is still implicitly involved through the material acceleration required for the pressure calculation on the control surface. Integration of (3.1) seemingly avoids this issue and yields the associated force impulse, $\boldsymbol{P}(t)$, as

$$\boldsymbol{P}(t) = -\rho \int_{V_f} \boldsymbol{u} \mathrm{d}V - \frac{1}{N-1} \rho \oint_{S_e} \boldsymbol{x} \times (\hat{\boldsymbol{n}} \times \boldsymbol{u}) \mathrm{d}S + \int^{t} \left( \oint_{S_e} \hat{\boldsymbol{n}} \boldsymbol{\cdot} \boldsymbol{B} \mathrm{d}S \right) \mathrm{d}t' \tag{3.3}$$

$$\equiv \boldsymbol{P}_{lm} + \boldsymbol{P}_{nv} + \boldsymbol{P}_{v}. \tag{3.4}$$

Hence, equation (3.3) contains no time derivatives and the numerical time integration required to compute the third term is less affected by errors related to the temporal resolution. Similar to CV approaches, spatial derivatives appear only on the external boundary (which need not coincide with the measurement volume boundaries). The terms $\boldsymbol{P}_{lm}$, $\boldsymbol{P}_{nv}$ and $\boldsymbol{P}_{v}$ represent force impulse contributions from total linear momentum, (asymptotically) non-vanishing and vanishing surface momentum fluxes, respectively.

## 4. Experimental details

The experimental set-up of Carr *et al.* (2013) is briefly reviewed here; the reader is referred to the paper for further details. The velocity data are for flow around rectangular, rigid flat plates of chord $c$ and span $b$, rotating at 45° angle of attack (figure 2*b*). The plates have aspect ratios ($\mathcal{R} = b/c$) 2 and 4, with $c = 6$ and 4.5 cm, and thickness-to-chord ratios of 5.3 and 3.5 %, respectively. Here, $Re = U_o c/\nu = 5000$, where $U_o = b\Omega_o$ is the maximum velocity of the plate tip with $\Omega_o$ as the maximum angular velocity and $\nu$ the kinematic viscosity of the fluid. The angular velocity programs are trapezoidal, with acceleration/deceleration over the intial/final 10° of the motion; the total rotation is 120° with period $T$.

The experiments were performed in a $91 \times 77 \times 71\ \mathrm{cm}^3$ glass-walled tank filled with a 50 % by mass glycerin–water mixture ($\nu \approx 5.11 \times 10^{-6}\ \mathrm{m}^2\ \mathrm{s}^{-1}$). The data sets were obtained from chordwise planes of phase-locked, phase-averaged (five realisations) S-DPIV measurements, and were acquired in an inertial frame which instantaneously coincides with a Cartesian frame with $x$- and $y$-axes parallel and normal, respectively, to the plate chord and $z$-axis along the plate span (figure 2*a*). For both cases, the volumetric data have spatial resolutions of $\Delta x = \Delta y = 1.8$ mm (in-plane) and $\Delta z = 3.6$ mm (out-of-plane), which yield approximate measurement volumes of $17c^3$ and $61c^3$ consisting of 36 and 54 planes of S-DPIV data for the $\mathcal{R} = 2$ and 4 cases, respectively. Owing to laser reflections from the plate clamp, the flow over a spanwise distance of 0.66 cm starting from the plate root was not measured. The stereoscopic view of the plate does not allow the flow in a thin region extending from the plate leading and trailing edges to be imaged. The data were acquired with a constant angular resolution of $\Delta\phi = 6°$, giving temporal resolutions of $\Delta t \approx 0.030$ s and 0.033 s for the $\mathcal{R} = 2$ and 4 cases, respectively; non-dimensionally these are $\Delta t U_o/c \approx 0.213$ and 0.416. Carr *et al.* (2013) performed a thorough error analysis on the experimental configuration and reported an estimate of the normalised velocity uncertainty as $\sim 0.01$ in-plane and twice this out-of-plane.

Forces are measured using a submersible ATI Nano 17-IP68, six-axis transducer that allows full-scale loads of 25 N and static uncertainties of $\sim 0.07$ % full scale and $\sim 0.63$ % of the measurement for the force axes. The plate inertia is analytically calculable and is subtracted from the transducer measurements. The component of the inertial force normal to the plate is only non-zero during the acceleration phases of the

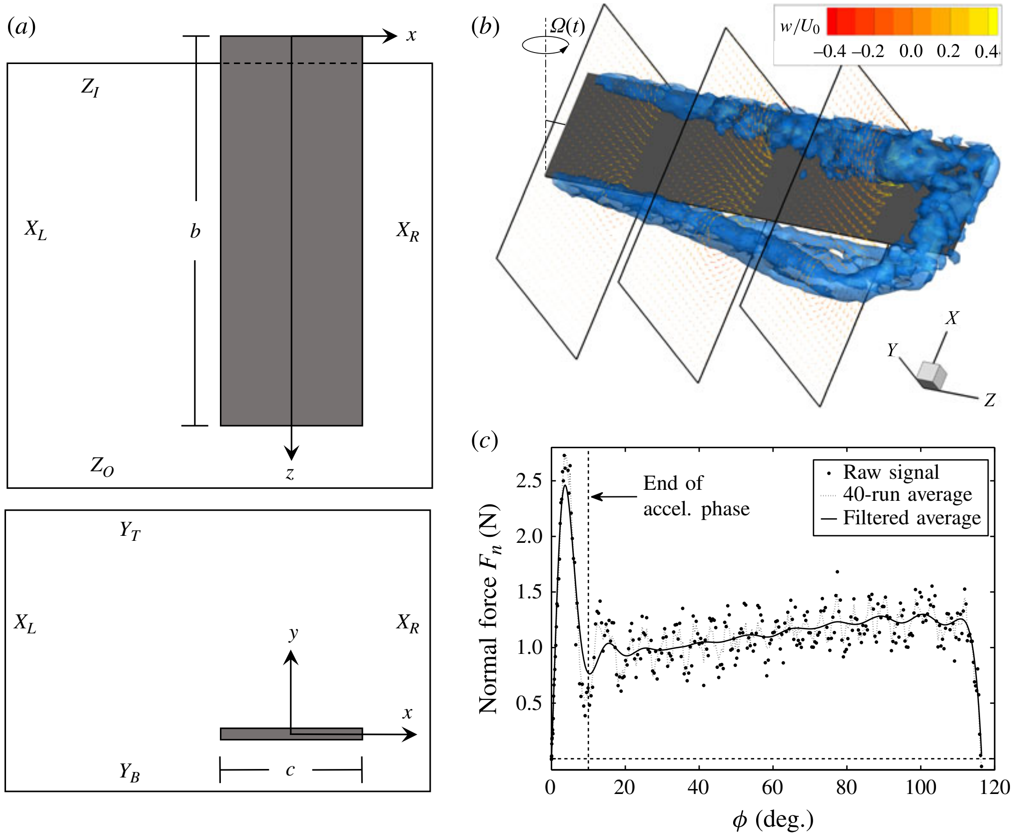

FIGURE 2. (Colour online) (*a*) The plate dimensions and approximate location in the measurement volume (not to scale). Also defined are the external boundaries (see § 5.2). (*b*) An example of a $Q$-criterion iso-surface at contour level one for the $\mathcal{R} = 4$ case at $\phi = 18^\circ$. Also shown are planes of three-component velocity vectors at 20, 50 and 80 % span, which are coloured by spanwise velocity. For clarity, the in-plane spacing of the vectors is $(2\Delta x, 2\Delta y)$ or twice the DPIV spacing, and the spatial extent of these planes has been reduced from that of the measurement volume. (*c*) Normal force traces, $F_n$, for raw, averaged and filtered average signals. For clarity, the data are cropped shortly after the plate deceleration phase begins.

motion and is $O(10^{-3})$ N which represents less than 5 % of the measured force. To help reduce mechanical vibrations, the accelerating portions of the velocity programs were replaced with hyperbolic tangents. The measurement is repeated 40 times and the averaged result is smoothed by a third-order Butterworth filter (figure 2*c*); cutoff frequencies of 35 and 18 Hz for the $\mathcal{R} = 2$ and 4 cases were determined from the power spectral density of the raw force signals. It is noteworthy that during the motion the mean difference between the force impulse computed from the averaged and the filtered average force signals is less than 0.1 %.

## 5. Results and discussion

A force impulse coefficient is defined as $\boldsymbol{P}^* = \boldsymbol{P}/\{(1/2\rho U_o^2 cb)T\}$, and is consistent with integrating a classical force coefficient over non-dimensional time $t/T$. Only the component normal to the plate, $P_n^*$, is examined as it is the largest. The ratio of the normal force signal power to the other components is almost 20 dB, and comprises nearly 98 % of the total power in the transducer data.

### 5.1. *Origin dependence*

The S-DPIV measurement frame is instantaneously at rest and so $\boldsymbol{u}_e \equiv \boldsymbol{0}$ in the equations of the previous sections. However, the results below are not dependent on this condition and can be easily modified to include non-zero $\boldsymbol{u}_e$. The explicit appearance of $\boldsymbol{x}$ in (3.3) requires an origin, say $\boldsymbol{x}_o$ (see figure 1), to be specified. Theoretically, the position origin is arbitrary, but the presence of errors in the data introduces an artificial dependence on $\boldsymbol{x}_o$.

#### 5.1.1. *Statistical considerations*

Let $\boldsymbol{P}_1$ be the collection of terms in (3.3) which contain $\boldsymbol{x}$ and $\boldsymbol{P}_2$ be that which do not. We allow the force impulse to have parametric dependence on $\boldsymbol{x}_o$ and write $\boldsymbol{P}(t; \boldsymbol{x}_o) = \boldsymbol{P}_1(t; \boldsymbol{x}_o) + \boldsymbol{P}_2(t)$. Consider a set of origins of which $\boldsymbol{x}_o$ is a member, then from (3.3) the mean of $\boldsymbol{P}$ over this set is

$$\overline{\boldsymbol{P}}(t; \boldsymbol{x}_o) = \boldsymbol{P}_1(t; \overline{\boldsymbol{x}}_o) + \boldsymbol{P}_2(t) = \boldsymbol{P}(t; \overline{\boldsymbol{x}}_o) \tag{5.1}$$

where $\overline{\boldsymbol{x}}_o$ is the mean of the set $\{\boldsymbol{x}_o\}$. Hence, the mean of any number of force impulses calculated from any number of different origins is equivalent to that calculated with the origin located at the mean of all origins. Note that $\{\boldsymbol{x}_o\}$ is an uncountably infinite set and so is a continuous parameter. More importantly, its probability distribution is at our behest. However, the uniform distribution is the only one that is statistically justifiable, as any other would require *a priori* knowledge of the likelihood of certain origins to yield more accurate results. In general, such details are not objectively known.

To verify (5.1), we approximate the continuous origin distribution as a discrete one, $\{\boldsymbol{x}_{o,k}\}$ with $k = 1 \ldots K$, and use $K = 1500$ origins uniformly distributed over the entire measurement volume. For $\mathcal{R} = 2$ and 4, $K$ represents 0.5 and 0.3 % of the gridded volumes. Then, $\overline{\boldsymbol{P}}(t; \boldsymbol{x}_{o,k})$ is directly calculated from the S-DPIV data using this discrete distribution. Also computed is $\boldsymbol{P}(t; \overline{\boldsymbol{x}}_o)$ with $\overline{\boldsymbol{x}}_o$ corresponding to the population mean of the continuous distribution, $\overline{\boldsymbol{x}}_o = (1/2)\{\max[\boldsymbol{x}_o] + \min[\boldsymbol{x}_o]\}$, and to the sample mean of the discrete distribution, $\overline{\boldsymbol{x}}_{o,k} = (1/K)\sum_{k=1}^{K} \boldsymbol{x}_{o,k}$. The results for $P_n^*$ are plotted in figure 3, which shows that the data are nearly indistinguishable; also shown are the transducer data. The root-mean-square (RMS) deviations of $\overline{P_n^*}(t; \boldsymbol{x}_{o,k})$ from $P_n^*(t; \overline{\boldsymbol{x}}_o)$ and $P_n^*(t; \overline{\boldsymbol{x}}_{o,k})$ are $O(10^{-4})$ and $O(10^{-16})$ (~machine zero), respectively. The extremely small error for the latter is due to the linear appearance of $\boldsymbol{x}$ in the equations as well as the linearity of the mean operator. The former is larger because $\overline{\boldsymbol{x}}_o = \overline{\boldsymbol{x}}_{o,k} + \delta\overline{\boldsymbol{x}}_{o,k}$, where the discretisation error, $\delta\overline{\boldsymbol{x}}_{o,k}$, is a difference of $\sim 0.05c$.

For $\mathcal{R} = 2$, $P_n^*$ is underpredicted throughout the motion, whereas for $\mathcal{R} = 4$, it is fairly well-predicted early on, but then continually deviates. At $\phi = 66^\circ$ there is a failure of the calculation indicated by a significant change of the slope in the data, and $P_n^*$ actually decreases after $\phi = 78^\circ$. This calculation failure is discussed further in § 5.1.2. The RMS deviations of $P_n^*$ from the transducer data are 29 and 38 % for $\mathcal{R} = 2$ and 4, respectively. Although there are certainly experimental errors in the S-DPIV measurements and numerical inaccuracies introduced into those data, these are unlikely, in and of themselves, to cause such large discrepancies. A more probable

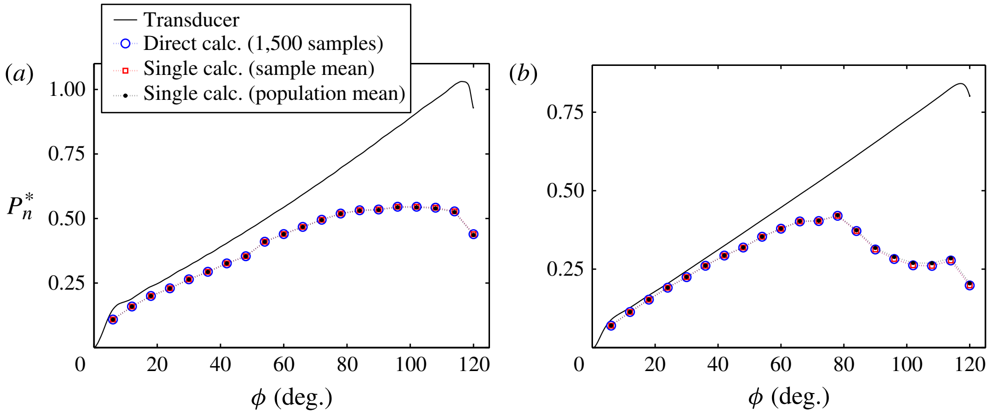

FIGURE 3. (Colour online) Normal component of force impulse, $P_n^*$, from the transducer and S-DPIV data plotted against rotational angle, $\phi$, for (*a*) $\mathcal{R} = 2$ and (*b*) $\mathcal{R} = 4$. The direct calculation is from the average of a set of uniformly distributed origins, and the single calculations are from one origin located at the mean of the set.

and insightful explanation is the amplification of these errors by the position vector, as is investigated next. Noca (1997) refers to this issue as the 'moment-arm dilemma' in connection to cross-multiplications involving $\boldsymbol{x}$.

Despite the consistency observed in figure 3, there is still no indication of the quality of the calculation other than the transducer data. Furthermore, without these data, failure of the calculation may not be so obvious, and therefore more information is needed about the reliability of the calculation. It is desirable to obtain further statistics and with minimal calculation so as to avoid computing a large discrete set of $\boldsymbol{P}(t; \boldsymbol{x}_{o,k})$. From (5.1) the force impulse deviation from the mean is

$$\boldsymbol{P}(t; \boldsymbol{x}_o) - \overline{\boldsymbol{P}}(t; \boldsymbol{x}_o) = \boldsymbol{P}_1(t; \boldsymbol{x}_o) - \boldsymbol{P}_1(t; \overline{\boldsymbol{x}}_o) = \mathsf{A} \boldsymbol{\cdot} (\boldsymbol{x}_o - \overline{\boldsymbol{x}}_o) \tag{5.2}$$

where $\mathsf{A}(t)$ is a tensor that depends only on time. By substituting (3.2) into (3.3) and the result into (5.2), then using the triple vector product to isolate the position vector terms, it is found that

$$\begin{aligned}\mathsf{A}(t) &= \frac{1}{N-1}\left\{\int^{t}\left(\oint_{S_e}[\hat{\boldsymbol{n}} \otimes (\rho \boldsymbol{u} \boldsymbol{\cdot} \nabla \boldsymbol{u} - \nabla \boldsymbol{\cdot} \boldsymbol{T}) - (\rho \boldsymbol{u} \boldsymbol{\cdot} \nabla \boldsymbol{u} - \nabla \boldsymbol{\cdot} \boldsymbol{T}) \otimes \hat{\boldsymbol{n}}]\mathrm{d}S\right)\mathrm{d}t' \right.\\ &\quad \left. + \rho \oint_{S_e}[\hat{\boldsymbol{n}} \otimes \boldsymbol{u} - \boldsymbol{u} \otimes \hat{\boldsymbol{n}}]\mathrm{d}S\right\}. \end{aligned} \tag{5.3}$$

Since $\boldsymbol{P}$ is theoretically invariant with $\boldsymbol{x}_o$, this requires $\mathsf{A} = \mathsf{D}_{\boldsymbol{x}_o}\boldsymbol{P}(t; \boldsymbol{x}_o) \equiv 0$; here the allowed non-zero $\mathsf{A}$ represents errors in the data, specifically those on the boundary $S_e$. The manner in which these errors are amplified by the position vector is clear from the right-hand side of (5.2) and the covariance matrix of $\boldsymbol{P}(t; \boldsymbol{x}_o)$ can be written as

$$\Sigma(\boldsymbol{P}) = \mathsf{A}\Sigma(\boldsymbol{x}_o)\mathsf{A}^{\mathrm{T}}, \tag{5.4}$$

where $\Sigma(\boldsymbol{x}_o)$ is the covariance matrix of $\boldsymbol{x}_o$ and matrix notation has been adopted for operations. Since one is most often interested in the components of $\boldsymbol{P}$, it seems more appropriate to investigate the scalar variances of these individual components.

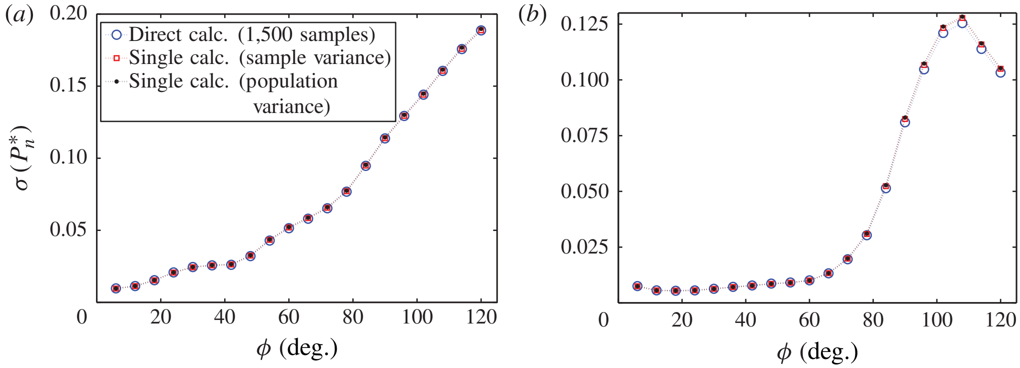

FIGURE 4. (Colour online) Standard deviation, $\sigma(P_n^*)$, versus $\phi$ for (*a*) $\mathcal{A\!R} = 2$ and (*b*) $\mathcal{A\!R} = 4$. The calculation methods are the same as those in figure 3.

By definition, these variances, $\mathrm{Var}(P_i)$, are given by the diagonal elements of $\boldsymbol{\Sigma}(\boldsymbol{P})$. Now, since $\boldsymbol{x}_o$ uniquely describes any point, its components must be independent (i.e. uncorrelated), and so the covariance of different components is zero. Thus, $\boldsymbol{\Sigma}(\boldsymbol{x}_o)$ is a diagonal matrix with entries corresponding to the scalar variances of each component of $\boldsymbol{x}_o$, $\mathrm{Var}(x_{o_i})$. It then follows that

$$\mathrm{Var}(P_i) = A_{ij}^2 \mathrm{Var}(x_{o_j}) \tag{5.5}$$

where summation notation is implied. Further inspection of (5.3) reveals that $\boldsymbol{A}$ is a skew-symmetric tensor and so its three independent elements are the components of a vector, say $\boldsymbol{a}$, subject to $A_{ij} = \epsilon_{ijk} a_k$, and whence (5.5) becomes

$$\mathrm{Var}(P_i) = (\epsilon_{ijk} a_k)^2 \mathrm{Var}(x_{o_j}) = \sum_{j \neq i} A_{ij}^2 \mathrm{Var}(x_{o_j}) \tag{5.6}$$

$$\therefore \sigma(P_i) = \sqrt{\sum_{j \neq i} A_{ij}^2 \mathrm{Var}(x_{o_j})}, \tag{5.7}$$

where $\sigma(P_i)$ is the standard deviation of the $i$th component of $\boldsymbol{P}$. Similar to (5.1) for the mean of $\boldsymbol{P}$, equation (5.7) only requires one calculation involving the experimental data (i.e. $\boldsymbol{A}(t)$) to determine the standard deviation of $P_i(t; \boldsymbol{x}_o)$ corresponding to a continuous distribution of origins, $\{\boldsymbol{x}_o\}$.

To validate (5.7), we again use the finite number ($K = 1500$) of $\boldsymbol{P}(t; \boldsymbol{x}_{o,k})$ obtained from the discrete origin distribution to directly calculate $\sigma(P_i)$. Also, the right-hand side of (5.7) is computed with $\mathrm{Var}(x_{o_i})$ corresponding to the population variance of the continuous distribution, $\mathrm{Var}(x_{o_i}) = (1/12)\{\max[x_{o_i}] - \min[x_{o_i}]\}^2$, and to the sample variance of the discrete distribution, $\mathrm{Var}(x_{o_i,k}) = (1/K-1)\sum_{k=1}^{K}(x_{o_i,k} - \bar{x}_{o_i,k})^2$. Figure 4 plots the results for $\sigma(P_n^*)$, and once again the data are in almost perfect agreement. The RMS deviations between each of the calculations are $O(10^{-4})$; here the machine zero value does not occur because of the nonlinear variance operator.

For both $\mathcal{A\!R}$ cases, $\sigma(P_n^*)$ is initially low, but steadily rises as the flow develops. Physically, this corresponds to a 'breakdown' event in the outboard main flow structure (Carr *et al.* 2013). Since the theoretical standard deviation of $P_i(t; \boldsymbol{x}_o)$ over a set of $\boldsymbol{x}_o$ is zero, one may then use the experimental $\sigma(P_i)$ as a quality indicator

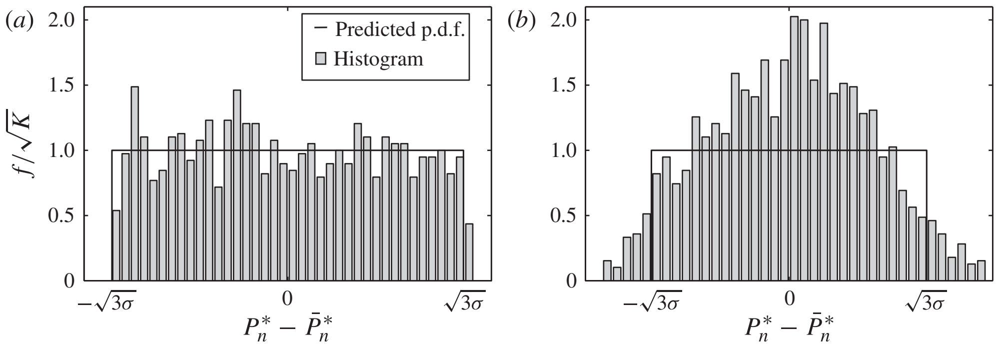

FIGURE 5. Normalised mean-shifted histogram and predicted p.d.f. of $P_n^*$ for (*a*) $\phi = 12^\circ$ and (*b*) $\phi = 96^\circ$ for $\mathcal{R} = 4$. The number of bins for the histograms is $\lceil\sqrt{K}\rceil = 39$. Note that the horizontal scale ratio of (*b*) to (*a*) is 25:1.

for the computed $\boldsymbol{P}$. For example, $\sigma(P_n^*)$ for the $\mathcal{R} = 4$ case rapidly increases after $\phi \approx 66^\circ$, which is consistent with the qualitative observation made earlier about this point indicating a failure of the calculation (see also § 5.1.2). Similar observations can be made about the $\mathcal{R} = 2$ case. The obvious drawback is the subjective determination of an appropriate threshold for $\sigma(P_i)$, above which the calculated $\boldsymbol{P}$ is unacceptable.

Additional insight is gained using the properties of the uniform distribution, for which the probability density function (p.d.f.) is only non-zero within $\pm\sqrt{3}$ standard deviations of the mean. Hence, we may assert that only a particular extent of the distribution of $\boldsymbol{P}(t; \boldsymbol{x}_o)$ is explained by $\boldsymbol{x}_o$, meaning that

$$\Pr[|P_i - \overline{P_i}| > \sqrt{3}\sigma(P_i)] \geqslant 0, \tag{5.8}$$

with equality only for errors that are truly uniformly distributed on the boundary. This condition is fairly well-approximated when flow structures are not crossing $S_e$, such as for the first several measurement times; at later times, the error distribution, and so $\boldsymbol{P}$, may display a non-uniform character. Therefore, in addition to an increase in $\sigma(P_i)$, the departure of the distribution of $\boldsymbol{P}$ from uniform can also help indicate increased error levels in the calculation. This is exemplified in figure 5, which shows histograms of $P_n^*$, as well as the predicted p.d.f. defined by the bracketed terms in (5.8) for small and large $\phi$. The standard deviation and the width of the histograms are equivalent as error indicators, but the shape of the distribution provides an additional, more objective indication of unexplained error. Note that the histogram does not require calculation of $\boldsymbol{P}(t; \boldsymbol{x}_{o,k})$, but only of $\boldsymbol{A}(t)$ and the generation of $\boldsymbol{x}_{o,k}$.

### 5.1.2. *Objective origin selection*

The analysis in § 5.1.1 provides easily obtainable statistical information about the variation of $\boldsymbol{P}$ with $\boldsymbol{x}_o$. However, the results are dependent on the extent of the specified origin distribution. For example, changing the intervals that define this distribution will result in a different mean origin and hence a different mean force impulse. Furthermore, the standard deviation will yield the same value for any origin distribution that has the same variance, regardless of the global spatial location of that distribution (i.e. $\overline{\boldsymbol{x}}_o$). Although (5.2) is valid for any two origins, an origin that minimises $\sigma(P_i)$ cannot be found since the deviation is relative, and we have no objective reason to believe either associated force impulse is accurate. We now show that satisfying an identity condition leads to improved results for $\boldsymbol{P}$.

Recall that the 'error tensor', $\boldsymbol{\mathsf{A}}$, is composed of terms which are amplified by the position vector. These terms are a direct result of the pressure removal, in which the material acceleration and viscous stress are substituted (see (3.1) and (3.2)). Since only the velocity is measured, all other flow quantities are calculated. Therefore, to mitigate this error amplification it would be ideal to relate the associated terms through conditions involving strictly the velocity. For the local acceleration (represented by $\boldsymbol{P}_{nv}$, see (3.4)), such a condition is achieved by letting $\boldsymbol{a}=\boldsymbol{u}$ in (2.1), and similarly for the convective acceleration with $\boldsymbol{a}=\nabla(\frac{1}{2}|\boldsymbol{u}|^2)$. These conditions are

$$(N-1)\int_{V_f}\boldsymbol{u}\,\mathrm{d}V=\int_{V_f}(\boldsymbol{x}-\boldsymbol{x}_o)\times\boldsymbol{\omega}\,\mathrm{d}V-\oint_S(\boldsymbol{x}-\boldsymbol{x}_o)\times\hat{\boldsymbol{n}}\times\boldsymbol{u}\,\mathrm{d}S \qquad (5.9a)$$

$$-(N-1)\oint_S\frac{1}{2}|\boldsymbol{u}|^2\hat{\boldsymbol{n}}\,\mathrm{d}S=\oint_S(\boldsymbol{x}-\boldsymbol{x}_o)\times\hat{\boldsymbol{n}}\times[\boldsymbol{u}\boldsymbol{\cdot}\nabla\boldsymbol{u}+\boldsymbol{u}\times\boldsymbol{\omega}]\,\mathrm{d}S, \qquad (5.9b)$$

and for completeness $S=S_b\cup S_e$, but the contributions from $S_b$ are exactly known. No condition exists for the viscous term, but its contribution is often negligible such as here with an average of less than 0.25 % of $P_n^*$. Since both of the above equations are theoretically invariant under $\boldsymbol{x}$, we define the 'objective origin', $\boldsymbol{x}_o$, as the one that best satisfies the summation of these equations on a component-wise basis. This is determined as the origin which yields the smallest RMS deviation (over time) between the left- and right-hand side. Note that random velocity measurement errors will affect the left-hand sides of (5.9), but spatial integration of these quantities leads to negligible error accumulation (see appendix A).

Figure 6 shows $P_n^*$ from the transducer and S-DPIV using the objective origin, as well as the individual contributions to $P_n^*$ from the three terms in (3.4). For $\mathcal{A}\!\!\!R=2$, the agreement of the S-DPIV data with the transducer throughout the motion is substantially improved compared with figure 3(*a*). For $\mathcal{A}\!\!\!R=4$, the agreement is slightly improved prior to $\phi\approx 66°$, however the calculation failure thereafter is still present. The RMS deviations of $P_n^*$ from the transducer data are now 4 and 23 % for $\mathcal{A}\!\!\!R=2$ and 4, respectively. Table 1 lists these RMS values along with those corresponding to figure 3 for comparison, and it is clear that the objective origin yields a significant improvement compared with the transducer data. The terms $\boldsymbol{P}_{lm}$ and $\boldsymbol{P}_{nv}$ together are equivalent to the hydrodynamic impulse of the fluid, and $\boldsymbol{P}_v$ represents momentum flux in the more usual sense. $P_v^*$ becomes non-negligible at $\phi\approx 24°$ for $\mathcal{A}\!\!\!R=2$, but not until $\phi\approx 72°$ for $\mathcal{A}\!\!\!R=4$, which makes sense given the larger relative spatial domain of the latter. The calculation failure of the $\mathcal{A}\!\!\!R=4$ case clearly affects $P_{nv}^*$ and $P_v^*$ as is evinced through their abrupt changes occurring at $\phi=66°$. Similar to the results of others, this is associated with flow structures crossing the outer boundaries.

The persistence of the calculation failure for the $\mathcal{A}\!\!\!R=4$ case suggests that these data contain a source of error other than random measurement noise and amplification. This additional error is caused by the outboard 'breakdown' of the flow for this case, which we believe to be transitional. More specifically, the outboard leading-edge vortex structure lifts off from the plate and eventually breaks down into a dispersed, less coherent structure. This process is likely not converged with only five realisations of S-DPIV data. Although transducer data of several other *Re* and $\mathcal{A}\!\!\!R$ cases indicate that this event has no significant effect on the force (Carr, DeVoria & Ringuette 2014), any non-repeatability weakens the validity of the S-DPIV volume reconstruction

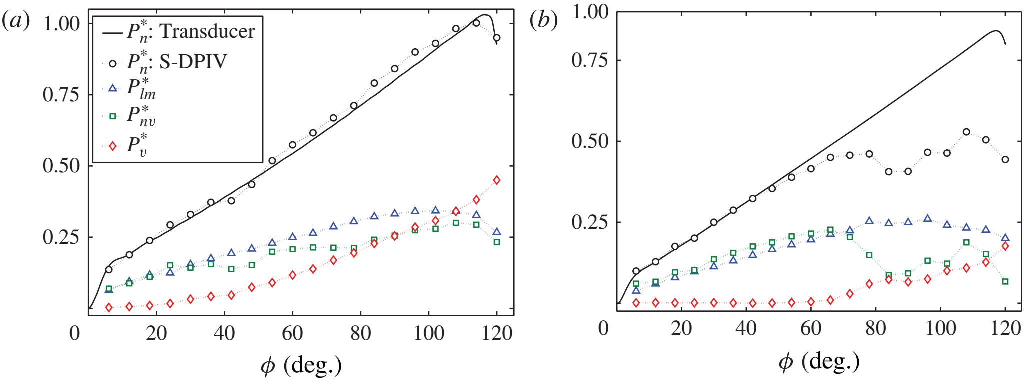

FIGURE 6. (Colour online) Plots of $P_n^*$ as calculated from the objective origin for (*a*) $Æ = 2$ and (*b*) $Æ = 4$. Also shown are the contributions to $P_n^*$ from linear momentum ($P_{lm}^*$), non-vanishing ($P_{nv}^*$) and vanishing ($P_v^*$) surface fluxes of momentum.

| Æ | Figure 3 (%) | Figure 6 (%) | RMS reduction (%) | $\beta$ (deg.) | $b/a$ |
|---|---|---|---|---|---|
| 2 | 29 | 4 | 90 | 3 | 0.05 |
| 4 | 38 | 23 | 41 | 30 | 0.26 |

TABLE 1. RMS deviations of $P_n^*$ from the transducer data for origins at the mean of the uniform distribution (figure 3) and the objective origin (figure 6), and the per cent reduction of the actual RMS values. Also, the angle $\beta$ between the RMS-axis and $\boldsymbol{v}$, and the minor-to-major axis ratio, $b/a$, of the RMS field elliptical contours.

for which each plane of data represents an independent measurement of the flow. This also applies to non-repeatability in phase-averaged, whole-volume tomographic DPIV measurements. In either case, even in the absence of measurement noise, the reconstructed data would not be completely consistent with the true flow. We must then make a distinction between these two sources. The amplified error related to measurement noise is simply referred to as noise amplification, while the other source is termed non-repeatability error and represents fluctuations in the flow occurring from different realisations of the experiment. Both types of error are susceptible to amplification by the position vector.

More insight into noise amplification and non-repeatability error may be gained by comparing the error tensor, $\boldsymbol{A}$, to the conditions given in (5.9) that determine the objective origin. The difference between two force impulses calculated from any two origins, say $\boldsymbol{x}_{o,1}$ and $\boldsymbol{x}_{o,2}$, is $\boldsymbol{A}\boldsymbol{v}$, where $\boldsymbol{v} = \boldsymbol{x}_{o,2} - \boldsymbol{x}_{o,1}$ (recall (5.2)). Errors in the data make $\boldsymbol{A}$ non-zero and $\boldsymbol{x}_{o,1} \neq \boldsymbol{x}_{o,2}$ by assumption and so the force impulse difference can be made zero only if $\boldsymbol{v} \in \ker(\boldsymbol{A})$. Since $\boldsymbol{A}$ is skew-symmetric, then $\exists\, \lambda \in \operatorname{spec}(\boldsymbol{A})$ such that $\lambda = 0$. Hence, the nullspace of $\boldsymbol{A}$ is equivalent to the eigenspace corresponding to $\lambda = 0$ and is guaranteed to be non-trivial. Recall $\boldsymbol{A} = \boldsymbol{D}_{\boldsymbol{x}_o}\boldsymbol{P}$, so that the (real) eigenvector $\boldsymbol{v}$ represents the direction in which changes in the force impulse are zero. Now, note that the *i*th components of $\boldsymbol{P}$ and (5.9) are independent of the *i*th component of the position vector. The RMS field used to determine the objective origin for $P_i$ can then be visualised as a surface with a domain defined by the remaining two components of $\boldsymbol{x}_o$. Here the RMS fields corresponding to $P_n^*$ are found to have a narrow minimum valley with essentially elliptical contours of eccentricities very near unity. This is, however, a general feature (see appendix B). Then, the direction in which changes in the RMS field are minimal is well-approximated by the vector along the ellipse's major axis; we refer to this as the RMS axis. Therefore, if the errors involved in computing $\boldsymbol{P}$ are dominated by noise amplification, then $\boldsymbol{v}$ will nearly coincide with the RMS axis.

Defining the angle between the RMS axis and the time average of $\boldsymbol{v}$ as $\beta$, it is found that $\beta = 3^\circ$ for $\mathcal{R} = 2$, which suggests that the error in this case is mostly due to noise amplification and thus explains the success of the objective origin in providing agreement between the S-DPIV and transducer data. Conversely, for $\mathcal{R} = 4$ $\beta$ is considerably larger at $30^\circ$ and, as mentioned previously, indicates a significant non-repeatability error leading to the calculation failure. However, repeating the calculations using only the data prior to $\phi = 66^\circ$ yields $\beta = 3.8^\circ$ and an RMS deviation from the transducer data over this range of 4 %. In practice, one could repeat such computations over a successively larger time range of data until an observable increase in $\beta$ occurs, thus indicating a transition of error type from noise amplification to non-repeatability. An origin that better corrects the calculation after the failure was found via trial-and-error, but the absence of an objective method to determine this origin strongly suggests the result is merely imposed and unphysical.

The eigenvector $\boldsymbol{v}$ describing one direction along which zero change occurs in $\boldsymbol{P}$ for any position explains the appearance of the RMS field contours as long, narrow regions. The minor-to-major-axis ratio, $b/a$, quantifies the narrowness of these RMS contours; $b/a = 0.05$ and 0.26 for $\mathcal{R} = 2$ and 4, respectively. Although the ratio for $\mathcal{R} = 4$ is approximately 5 times that of $\mathcal{R} = 2$, both are small enough to make the direction defined by the major axis, i.e. the RMS axis, unambiguously distinct.

### 5.2. *Boundary dependence*

Previously we used the entire measurement volume for any calculations. Theoretically the size and shape of the boundary are inconsequential to the force, so long as $S_e$ encloses the body. This is obvious from the limit as $S_e \to S_b$ of any of the equations in § 2 which will yield an identity of $\boldsymbol{F}$ as the surface integral of the total stress on the body. However, $\boldsymbol{A}$ assumes a parametric dependence on $S_e$ via its surface integral definition (see (5.3)), which is non-zero because of errors in the data. In other words, the artificial dependence of $\boldsymbol{P}$ (and $\boldsymbol{F}$) on $S_e$ arises for the same reasons as origin dependence, and the two create identical effects. Hence, the objective origin defined in § 5.1.2 can be used at each change of $S_e$ to minimise noise amplification.

#### 5.2.1. *External boundary*

In this section the objective origin method is investigated for consistency of results with varied $S_e$. We define the bounding surfaces of the rectangular measurement volume as $X_L$, $X_R$, $Y_T$, $Y_B$, $Z_I$ and $Z_O$ where the subscripts denote left, right, top, bottom, inboard and outboard (see figure 2*a*). The results are interpreted through the RMS deviations of $P_n^*$ from the transducer data.

We begin with the in-plane boundary surfaces $X_L$, $X_R$, $Y_T$ and $Y_B$, and $S_e$ is altered by allowing one surface to progressively encroach inward until the plate is reached, while all others remain fixed at their most outward locations. After each repositioning of the boundaries the objective origin is recalculated. Figure 7 plots the corresponding RMS values, and for clarity only results below a certain value are shown as some are in excess of 175 % when very near the plate. Also, for the $x$-plane

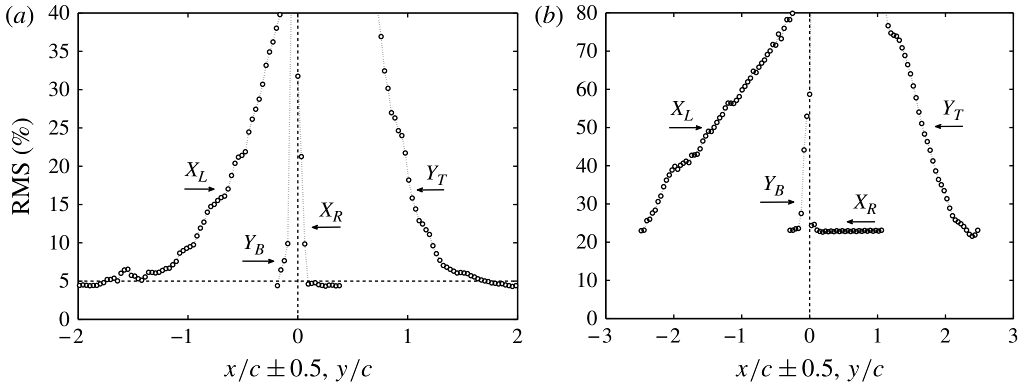

FIGURE 7. RMS deviations of $P_n^*$ from the transducer data for changes of the in-plane boundaries for (*a*) $A\!\!\!R = 2$ and (*b*) $A\!\!\!R = 4$. The arrows indicate the direction of inward movement of the specified surface. The horizontal dashed line in (*a*) marks 5 %.

surfaces $X_R$ and $X_L$, the abscissa is shifted so that the zero position corresponds to the leading and trailing edge, respectively, of the plate. For $A\!\!\!R = 4$, the errors begin to increase almost immediately for all boundaries except $X_R$, for which the error remains nearly constant, likely because this boundary is ‘upstream’ of the plate and so noisy flow structures do not cross it. The continually increasing errors are not surprising for this case because of the calculation failure. However, for $A\!\!\!R = 2$ the errors are initially nominally constant near their lowest levels, which correspond to the largest domain size (i.e. figure 6*a*). As figure 7(*a*) indicates, the errors are below 5 % for approximately 0.5 chords of inward travel of the boundaries. This shows that the objective origin is successful in mitigating noise amplification errors until the boundaries are a certain distance away from the plate. For $X_L$ and $Y_T$, which have the majority of flow structure crossings, this distance is approximately $1.5c$, while for $X_R$ it is only $\sim 0.1c$ from the leading edge, and each of the errors increases rapidly upon further enclosing of $S_e$. The most outward location of $Y_B$ is $0.29c$ and it also has some flow structure crossings, thus explaining why this error increases right away.

For both $A\!\!\!R$ cases, the increases of the RMS deviation are caused by two, combinatory effects. First, as pointed out by Mohebbian & Rival (2012), when $S_e$ becomes smaller and closer to the body, a larger portion of the bounding surfaces have flow structures crossing them. Hence, the noise on $S_e$ is significantly increased and susceptible to amplification. Second, flow structures will cross the surfaces at earlier times and so when noise amplification becomes very large the S-DPIV data will be in disagreement with the transducer for longer periods of time.

Even at its most outward position $Z_I \subset S_e$ intersects the plate near the root (see figure 2*a*). Technically, if $S_e$ does not entirely enclose the body, then the comparison of flow field data with the actual force on the body is physically inconsistent. However, by moving $Z_I$ further inward we may assess the consequence of the missing region of flow near the root of the plate, which for the $A\!\!\!R = 2$ and 4 plates is 5.5 and 3.7 % of the respective spans (see § 4). Neglecting this small portion of the flow in the calculation should have a minor effect. This is because the azimuthal velocity of the plate is lowest near the root and so the total stress, particularly the pressure differential, is likely to be small there.

The $Z_I$ boundary is made to traverse along the entire length of the domain and figure 8 plots the corresponding data showing that for initial displacements of the

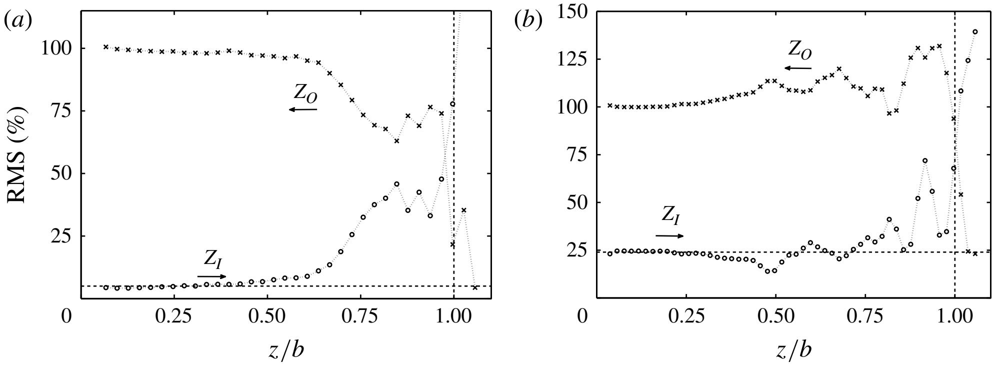

FIGURE 8. RMS deviations of $P_n^*$ from the transducer data for changes of the $z$-plane boundaries for ($a$) $\mathcal{R}=2$ and ($b$) $\mathcal{R}=4$. The arrows indicate the direction of inward movement of the specified surface. The vertical dashed lines mark the plate tip at $z/b=1$, and the horizontal lines mark 4 % for ($a$) and 23 % for ($b$); see table 1.

boundary the RMS values remain very close to those listed in table 1. This supports the assertion that the missing region of flow near the plate root has little effect on the calculation. However, the fact that the errors are near these values for locations of $Z_I$ as large as 30 and 55 % span for $\mathcal{R}=2$ and 4 is most likely a feature of the particular cases studied here, in which the flow structures near the root (i.e. leading-edge and trailing-edge vortices) are fairly symmetrical (see Carr *et al.* 2013). Figure 8 shows that this symmetry is also apparent in the data for $Z_O$, which are essentially a mirror image of the $Z_I$ data.

### 5.2.2. *Internal boundary*

Mohebbian & Rival (2012) conducted a numerical study on a two-dimensional flat plate at zero incidence to a $Re=1600$ freestream with a periodic vertical gust velocity. They employed a CV method that uses only control surface terms, and forces were computed for several different CV sizes which agreed well with those obtained from the total stress on the plate. Their calculations only slightly suffered when flow structures cross the boundary. The CV method used by Mohebbian & Rival (2012) is analogous to the 'flux equation' of Noca *et al.* (1999) in which the pressure is circumvented. Noca *et al.* (1999) showed similar agreement between forces obtained from the 'flux equation' and surface stresses determined from numerical data of a two-dimensional oscillating circular cylinder at $Re=100$, but using the experimental data of Noca, Shiels & Jeon (1997) they found inconsistency of the results when the position origin or the CV size was altered. They attributed this to three-dimensionality and the 'moment-arm dilemma,' which here we call noise amplification.

For many experiments it can be difficult to obtain high-quality, near-body measurements, and bypassing this task with a 'flux method' seems logical; several authors have reasonably stated this as justification for such methods. On the other hand, any 'flux method' will suffer from noise amplification, as the substitution

$$\int_{V_f} \boldsymbol{u}\,\mathrm{d}V = \oint_S \hat{\boldsymbol{n}} \cdot (\boldsymbol{u} \otimes \boldsymbol{x})\,\mathrm{d}S \tag{5.10}$$

is inherently relied upon. In fact, Mohebbian & Rival (2012) found that upon coarsening the grid of their simulation data to that of typical DPIV spatial resolutions, the accuracy of the calculations worsened as the domain size increased. Note that use

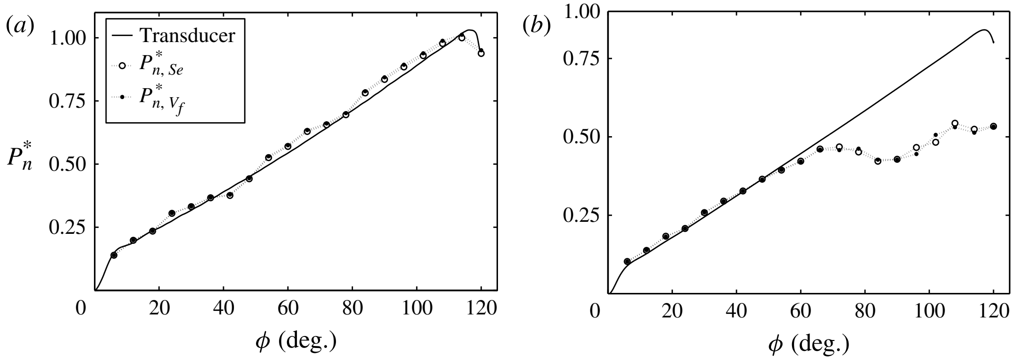

FIGURE 9. Plots of $P^*_n$ calculated from the 'flux method' and using objective origins corresponding to conditions involving only surface integrals, $P^*_{n,S_e}$, and both surface and volume integrals, $P^*_{n,V_f}$, for (*a*) $Æ = 2$ and (*b*) $Æ = 4$.

of (5.10) requires incompressibility, and again that $S = S_b \cup S_e$, where the contribution from $S_b$ is equivalent to the inertia of the fluidic body.

The 'flux method' is first assessed via its direct implementation, which is accomplished by replacing the total linear momentum, $\boldsymbol{P}_{lm}$, in (3.3) with (5.10). The form of the method employed should dictate the identity conditions used to determine the objective origin and, depending on the data available, any term in the equation for $\boldsymbol{P}$ (or $\boldsymbol{F}$) that has an identity relation to a term strictly involving the velocity should be used. However, use of a 'flux method' may imply that only data on $S_e$ are available and in this case the objective origin conditions should be modified to include just (5.9*b*), which only requires surface integrals.

Figure 9 plots $P^*_n$ from the transducer and S-DPIV using the 'flux method' with objective origins determined from just (5.9*b*), denoted as $P^*_{n,S_e}$, and from both of (5.9) with (5.10) as well, denoted as $P^*_{n,V_f}$. Both calculations yield similar results. For $Æ = 4$ the largest differences occur after $\phi = 66°$, when non-repeatability error dominates, which the objective origin cannot account for. Furthermore, $P^*_{n,S_e}$ and $P^*_{n,V_f}$ are comparable to the $P^*_n$ in figure 6, which were obtained from (3.3). For $Æ = 2$, the RMS deviations of $P^*_{n,S_e}$ and $P^*_{n,V_f}$ from the transducer data are 4.6 and 5 %, respectively, while for $Æ = 4$ these values are both 21 %. These errors are close to those listed in table 1 for figure 6, demonstrating the feasibility of a 'flux method.' However, this is not surprising as the methods are related by vector/integral identities (also see § 5 of Noca *et al.* 1999) and the noise on $S_e$, which is mitigated by the objective origin, remains the same.

We now assess the 'flux method' indirectly by returning to (3.3) for $\boldsymbol{P}$, but allow $S_b$ to progressively expand by removing data near the plate. This represents an increasing region of unimaged flow or invalidated measurements caused by, for example, reflections, shadows and perspective. One data point surrounding the plate is randomly selected for permanent deletion, the force impulse calculation performed, and the process repeats until a 'layer' of data around the plate is depleted; this is done for two layers. Also, we only consider the in-plane coordinates such that for each selected $(x_b, y_b) \in S_b$, the entire range of $z_b$ is removed; namely, spanwise rows of data are deleted. The origin and $S_e$ are fixed as the objective origin and the boundary of the largest domain, as in § 5.1; these choices yielded the lowest RMS deviation, denoted as $\mathrm{RMS}_o$.

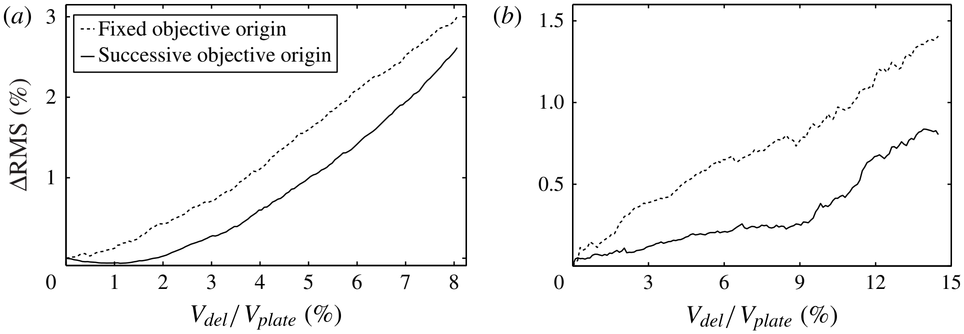

FIGURE 10. Shifted RMS deviations of $P_n^*$ from the transducer data for an increasing region of removed data, $V_{del}$, near the plate for (*a*) $\mathcal{R} = 2$ and (*b*) $\mathcal{R} = 4$. The shift value is $\text{RMS}_o = 4\,\%$ and $20\,\%$ for (*a*) and (*b*), respectively.

The results are again interpreted through the RMS deviations of $P_n^*$ from the transducer data, and are presented in figure 10 (dashed lines), where the dependent axis is $\Delta\text{RMS} \equiv \text{RMS} - \text{RMS}_o$ and the independent axis is the volume ratio of the deleted neighbourhood of data, $V_{del}$, to that of the plate, $V_{plate}$. As would be expected, the RMS continually increases as more data are removed. For $\mathcal{R} = 2$, the error begins to quickly grow even for small ratios of deleted data ($V_{del}/V_{plate} < 10\,\%$). This is because the removed data, being proximal to the moving plate, possess large momentum. For $\mathcal{R} = 4$ the error increase is less, because the flow ‘breakdown’ causes non-repeatability errors throughout the measurement volume and these are more significant than those due to data loss near the plate.

The same calculations are repeated, but the objective origin is successively implemented after each data removal. The results are also given in figure 10 (solid lines) and show that the error is consistently reduced. Of course the error must still have an increasing trend, because important flow data are removed. Although the decrease in error is only by a value of approximately 1 %, recall that the fixed origins correspond to those used for figure 6 and so the newly calculated origins are only slightly displaced from the preceding ones. Regardless, figure 10 is further evidence that the objective origin method, the definition of which has physical meaning, provides more accurate calculations by attenuating the amplified noise in the data.

### 5.3. *Force estimation*

Having calculated data for $\boldsymbol{P}$, there are several ways to estimate the force, $\boldsymbol{F}$. Here, we implement a standard centred finite difference (FD), as well as the least squares (LSQ) method to fit a high-order polynomial to the force impulse data, which is then differentiated. The force impulse data used are those in figure 6 and $P_n^*$ is associated with the normal force component, $F_n^*$. Also, since the current experiments are starting flows, we take advantage of the fact that $\boldsymbol{P}(t = 0) = \boldsymbol{0}$.

Figure 11 plots $F_n^*$ from the transducer as well as from the FD and LSQ methods for the S-DPIV data. Both methods produce similar results and the LSQ data are essentially a smoothed version of the FD data. The acceleration/deceleration phases occur over the first/last 10° of the plate motion, but the angular resolution of the S-DPIV data is $\Delta\phi = 6°$, with the first measurement at $\phi = 6°$. Hence, we cannot expect to capture the non-circulatory force peaks with acceptable accuracy. For $\mathcal{R} = 2$,

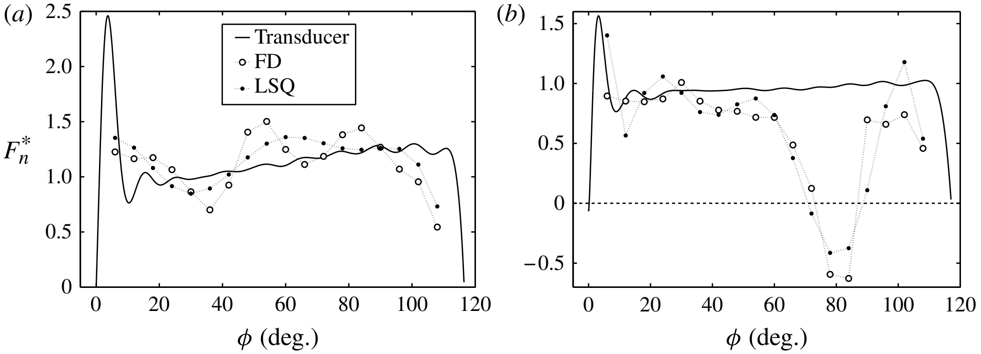

FIGURE 11. Normal force coefficient, $F_n^*$, from the transducer and S-DPIV data for (*a*) $Ꜳ = 2$ and (*b*) $Ꜳ = 4$. For clarity, data for $\phi > 108°$ have been omitted.

the prediction of $F_n^*$ through the majority of the constant velocity phase is reasonable, and likewise for $Ꜳ = 4$ prior to the calculation failure at $\phi \approx 66°$. The behaviour of $F_n^*$ may of course be inferred from the slope of $P_n^*$.

As expected the actual force computation is sensitive to the temporal resolution. This is not only true for computing the numerical derivative, but also and more importantly, for obtaining accurate values of $\boldsymbol{P}$. Although the current method (3.3) avoids time derivatives, it still relies on computation of the material acceleration, which is directly linked with the pressure gradient. Several techniques for improving the computation of the material acceleration have been developed recently and typically time-resolved (TR) data are essential for their implementation. For example, Novara & Scarano (2013) used three-dimensional tomographic TR-DPIV to perform particle tracking velocimetry (PTV) over a large number of image recordings. The method benefits from accurate trajectory reconstructions, as well as the higher spatial resolution of tomographic DPIV compared with conventional PTV. They report a significant reduction of precision errors and a near absence of truncation errors. Another technique is the 'pyramid correlation' developed by Sciacchitano, Scarano & Wieneke (2012), which greatly increases the signal-to-noise ratio of the particle image correlation leading to a decrease in the errors when the material acceleration is computed.

## 6. Concluding remarks

The practical implementation of calculating the force on a moving body, $\boldsymbol{F}$, from experimental flow field information was investigated. The flow data were obtained from S-DPIV volume reconstructions, and forces were directly measured with a transducer. To avoid introducing further errors into the data with numerical time derivatives, an equation for the force impulse, $\boldsymbol{P}$, was used in the majority of the work. This equation also avoids the explicit evaluation of the pressure on the external boundary. However, the associated substitutions still rely on computation of the material acceleration in a direct manner through the convective contribution, and indirectly through an integral term representing the local acceleration. The pressure removal introduces the explicit appearance of the position vector in the equations. Any errors in the data introduce an artificial dependence of the calculations on the position origin and, furthermore, these errors are also amplified by the position vector. This amplification is akin to the propagation error that is incurred through the spatial integration of the pressure gradient when the pressure is evaluated directly, and the choice of reference pressure location, from which the integration begins, is the analogue of origin dependence.

Considering a continuous uniform distribution of origins of any extent, it was shown that the mean and standard deviation of $\boldsymbol{P}$ over this set may each be obtained from a single calculation with the data. The standard deviation, along with the distribution of $\boldsymbol{P}$ can be used as error indicators for the quality of the force impulse calculation. However, these statistics are dependent on the prescribed extent of the origin distribution.

A distinction between two types of error, designated as noise amplification and non-repeatability error, was made. The former refers to random velocity measurement noise that is superimposed on the true velocity, and the latter is error which affects the validity of the volume reconstructions from independent S-DPIV data planes. Both types of error are subject to amplification via multiplication with the position vector. The definition of the angle $\beta$ quantifies the relative dominance of these errors, where small or near-zero values indicate noise amplification and larger values imply non-repeatability. This angle provides a metric by which the quality of the data for computing forces is acceptable. Non-repeatability error can be avoided with volumetric velocimetry techniques, which yield an entire volume of data as one independent measurement. However, the common practice of phase-averaging will reintroduce this type of error.

When noise amplification is dominant, the error may be attenuated. We proposed a method that objectively determines an origin which reduces the unphysical effects due to origin dependence associated with noise amplification. The method was termed the ‘objective origin’ and uses vector/integral identities that relate the velocity measurements to subsequently calculated amplified noise terms. A significant improvement in the calculations was observed as evinced by a large reduction in the RMS deviations of the S-DPIV data from the transducer. The objective origin was also shown to effectively mitigate noise amplification errors for changes in the external and internal boundaries.

Lastly, the computed data for $\boldsymbol{P}$ were used to obtain an estimate of $\boldsymbol{F}$. Reasonable agreement in the force magnitude was observed. Although the force impulse method used here avoids time derivatives and the direct evaluation of the pressure, the material acceleration must still be computed. In other words, the effect of temporal resolution cannot be avoided completely. It is well-known that accurately computing the pressure from velocity data is challenging and so any force method will suffer from the associated difficulties, regardless of whether or not the pressure is analytically removed. Although time-resolved data will yield more accurate estimations of the material acceleration, and therefore of force impulse, force or the pressure field, noise amplification is still possible. Thus, the objective origin method presented here is then a generally applicable technique to minimise noise amplification.

## Acknowledgements

This work was supported in part by the U.S. Air Force Office of Scientific Research grant FA9550-10-1-0281, supervised by Dr Douglas Smith.

## Appendix A. Velocity errors in the ‘objective origin’

The identities in (5.9) were used to determine the objective origin by minimising the RMS deviation of the summation of the equations. However, the left-hand sides, consisting of integrals involving only the velocity, may be affected by the random measurement errors as well. Let the measured velocity be decomposed as $\boldsymbol{u}=\boldsymbol{u}_T+\delta\boldsymbol{u}$, where $\boldsymbol{u}_T$ is the true velocity and $\delta\boldsymbol{u}$ the measurement error. The error in computing the left-hand side of (5.9*a*) is simply

$$\int_{V_f} \delta\boldsymbol{u}\,\mathrm{d}V, \tag{A 1}$$

and is negligible since the integration of a random error over a sufficiently large domain, such as $V_f$, tends to zero; the measurement volumes for the $\mathcal{R}=2$ and 4 cases consist of approximately 330 000 and 496 000 grid points, respectively.

For (5.9*b*), the situation is slightly more complex because of the nonlinear term $|\boldsymbol{u}|^2=|\boldsymbol{u}_T|^2+2\boldsymbol{u}_T\boldsymbol{\cdot}\delta\boldsymbol{u}+|\delta\boldsymbol{u}|^2$. The associated error is

$$\oint_{S_e} (\boldsymbol{u}_T\boldsymbol{\cdot}\delta\boldsymbol{u})\,\hat{\boldsymbol{n}}\,\mathrm{d}S+\oint_{S_e}\frac{1}{2}|\delta\boldsymbol{u}|^2\hat{\boldsymbol{n}}\,\mathrm{d}S. \tag{A 2}$$

The integrand of the first integral may be considered a random error and so its integrated contribution negligible, although the argument is perhaps not as strong as that for (A 1). However, with respect to the integration, the sign of the dot product creates an additional randomness and so accumulation of errors is likely to be small. For the second integral, let the velocity error be characterised by a representative value, say $\delta u>0$, which yields

$$\left|\oint_{S_e}\frac{1}{2}|\delta\boldsymbol{u}|^2\hat{\boldsymbol{n}}\,\mathrm{d}S\right|\leqslant\frac{1}{4}(\delta u)^2 S_e \tag{A 3}$$

since $S_e$ is an enclosure. Carr *et al.* (2013) performed a thorough error analysis on the experimental configuration and reported an estimate of the (normalised) velocity error as $\delta u=0.01$. Using the largest measurement domains for values of $S_e$, equation (A 3) yields very conservative errors of $4.2\times10^{-4}$ and $1.5\times10^{-3}$ for the $\mathcal{R}=2$ and 4 cases, respectively, and are also considered negligible.

Hence, provided that the experiment is carefully conducted to minimise the measurement error, then the quantities on the left-hand sides of (5.9) will be calculated with fair accuracy. This provides justification that the definition of the objective origin has a physically meaningful implication.

## Appendix B. Contours of the RMS field

In § 5.1 it was stated that the data produced elongated elliptical contours in the RMS field corresponding to the summation of (5.9). In this appendix we show that this is a general feature that arises as a result of the RMS-based definition of the objective origin, and is not specific to these data. The sum of (5.9) can be written as

$$\boldsymbol{A}=\boldsymbol{B}+\boldsymbol{C}\times\boldsymbol{x}_o, \tag{B 1}$$

where

$$\boldsymbol{A}(t)=(N-1)\left[\int_{V_f}\boldsymbol{u}\,\mathrm{d}V-\oint_S\frac{1}{2}|\boldsymbol{u}|^2\hat{\boldsymbol{n}}\,\mathrm{d}S\right], \tag{B 2}$$

$$\boldsymbol{B}(t)=\int_{V_f}\boldsymbol{x}\times\boldsymbol{\omega}\,\mathrm{d}V+\oint_S\boldsymbol{x}\times\hat{\boldsymbol{n}}\times[\boldsymbol{u}\boldsymbol{\cdot}\nabla\boldsymbol{u}+\boldsymbol{u}\times\boldsymbol{\omega}-\boldsymbol{u}]\,\mathrm{d}S, \tag{B 3}$$

$$\boldsymbol{C}(t)=\int_{V_f}\boldsymbol{\omega}\,\mathrm{d}V+\oint_S\hat{\boldsymbol{n}}\times[\boldsymbol{u}\boldsymbol{\cdot}\nabla\boldsymbol{u}+\boldsymbol{u}\times\boldsymbol{\omega}-\boldsymbol{u}]\,\mathrm{d}S. \tag{B 4}$$

Note that in the absence of errors $\boldsymbol{A} \equiv \boldsymbol{B}$, and $\boldsymbol{C} \equiv \boldsymbol{0}$ since the equations must be true for any $\boldsymbol{x}$. The component-wise definition of the objective origin is chosen because since 98 % of the transducer power is from the normal component, the other components are essentially noise, and so an attempt to compute these from the flow field will suffer from a substantially lower signal-to-noise ratio in those data. Therefore, a vector-based definition for the objective origin would make an unnecessary inclusion of such noise and bias the objective origin calculation. Now, the RMS of the third component is arbitrarily chosen for consideration. Also, for reasons apparent below we let $\boldsymbol{x}_o = (x, y, z)^{\mathrm{T}}$, and from (B 1) we obtain

$$\mathrm{RMS}^2 = \langle [(A_z - B_z) - (C_x y - C_y x)]^2 \rangle. \tag{B 5}$$

The components of $\boldsymbol{A}$, $\boldsymbol{B}$ and $\boldsymbol{C}$ are now assumed to be uncorrelated and to then represent mean values over time. This assumption is justified when the errors are mainly due to noise amplification, but becomes invalid when non-repeatability is significant. This is the reason that the objective origin can only handle the former type of error. After some algebra, expanding the right-hand side will yield

$$\mathrm{RMS}^2 + (B_z - A_z)^2 = [C_y x - (B_z - A_z)]^2 + [C_x y - (A_z - B_z)]^2 - 2C_x C_y xy. \tag{B 6}$$

The right-hand side of (B 6) can be separated into the following two equations

$$E = \left(\frac{x'}{a}\right)^2 + \left(\frac{y'}{b}\right)^2 \tag{B 7}$$

$$\psi = kxy, \tag{B 8}$$

where

$$x' = x - \left(\frac{B_z - A_z}{C_y}\right), \quad y' = y - \left(\frac{A_z - B_z}{C_x}\right), \tag{B.9a,b}$$

$$a = \frac{1}{C_y}, \quad b = \frac{1}{C_x}, \quad \text{and} \quad k = -2C_x C_y. \tag{B.10a–c}$$

Since (B 7) is the equation of an ellipse with a contour value of $E$, the reason for the ellipticity in the RMS field contours is apparent. Furthermore, equation (B 8) is a rectangular hyperbola, which is perhaps more recognisable as the stream function for potential stagnation point flow, where the asymptotes of the hyperbolae represent the principal axes of the rate-of-strain tensor (Batchelor 1967). Hence, the superposition of the function $\psi$ with the ellipse acts to stretch the latter and explains the general appearance of highly eccentric contours.

## REFERENCES

Batchelor, G. K. 1967 *An Introduction to Fluid Dynamics*. Cambridge University Press.

Carr, Z. R., Chen, C. & Ringuette, M. J. 2013 Finite-span rotating wings: three-dimensional vortex formation and variations with aspect ratio. *Exp. Fluids* **54**, 1444.

Carr, Z. R., DeVoria, A. C. & Ringuette, M. J. 2014 Aspect ratio effects on rotating wings: leading-edge circulation and forces. *J. Fluid Mech.*, (submitted).

David, L., Jardin, T., Braud, P. & Farcy, A. 2012 Time-resolved scanning tomogrpahy PIV measurements around a flapping wing. *Exp. Fluids* **52**, 857–864.

DAVID, L., JARDIN, T. & FARCY, A. 2009 On the non-instrusive evaluation of fluid forces with the momentum equation approach. *Meas. Sci. Technol.* **20**, 095401.

DEVORIA, A. C. & RINGUETTE, M. J. 2013 On the flow generated on the leeward face of a rotating flat plate. *Exp. Fluids* **54**, 1495.

HOWE, M. S. 2007 *Hydrodynamics and Sound*. Cambridge University Press.

JARDIN, T., DAVID, L. & FARCY, A. 2009 Characterization of vortical structures and loads based on time-resolved PIV for asymmetric hovering flapping flight. *Exp. Fluids* **46**, 847–857.

KURTULUS, D. F., SCARANO, F. & DAVID, L. 2007 Unsteady aerodynamic forces estimation on a square cylinder by TR-PIV. *Exp. Fluids* **42**, 185–196.

LEONARD, A. & ROSHKO, A. 2001 Aspects of flow-induced vibration. *J. Fluids Struct.* **15**, 415–425.

LIGHTHILL, J. 1986 Fundamentals concering wave loading on offshore structures. *J. Fluid Mech.* **173**, 667–681.

LIN, J.-C. & ROCKWELL, D. 1996 Force identification by vorticity fields: techniques based on flow imaging. *J. Fluids Struct.* **10**, 663–668.

LU, Y. & SHEN, G. X. 2008 Three-dimensional flow structures and evolution of the leading-edge vortices on a flapping wing. *J. Expl Biol.* **211**, 1221–1230.

MOHEBBIAN, A. & RIVAL, D. E. 2012 Assessment of the derivative-moment transformation method for unsteady-load estimation. *Exp. Fluids* **53**, 319–330.

NOCA, F. 1997 On the evaluation of time-dependent fluid-dynamic forces on bluff bodies. PhD thesis, Graduate Aeronautical Laboratories, California Institute of Technology, Pasadena.

NOCA, F., SHIELS, D. & JEON, D. 1997 Measuring instantaneous fluid dynamic forces on bodies, using only velocity fields and their derivatives. *J. Fluids Struct.* **11**, 345–350.

NOCA, F., SHIELS, D. & JEON, D. 1999 A comparison of methods for evaluating time-dependent fluid dynamic forces on bodies, using only velocity fields and their derivatives. *J. Fluids Struct.* **13**, 551–578.

NOVARA, M. & SCARANO, F. 2013 A particle-tracking approach for accurate material derivative measurements with tomogrpahic PIV. *Exp. Fluids* **54**, 1584.

OZEN, C. A. & ROCKWELL, D. 2012 Three-dimensional vortex structure on a rotating wing. *J. Fluid Mech.* **707**, 541–550.

POELMA, C., DICKSON, W. B. & DICKINSON, M. H. 2006 Time-resolved reconstruction of the full velocity field around a dynamically-scaled flapping wing. *Exp. Fluids* **41**, 213–225.

RANGI, D., VAN OUDHEUSDEN, B. W. & SCARANO, F. 2011 3D pressure imaging of an aircraft propeller blade-tip flow by phase-locked stereoscopic PIV. *Exp. Fluids* **52**, 463–477.

SAFFMAN, P. G. 1992 *Vortex Dynamics*. Cambridge University Press.

SÄLLSTRÖM, E. & UKEILEY, L. 2014 Force estimation from incompressible flow field data using a momentum balance approach. *Exp. Fluids* **55**, 1655.

SCIACCHITANO, A., SCARANO, F. & WIENEKE, B. 2012 Multi-frame pyramid correlation for time-resolved PIV. *Exp. Fluids* **53**, 1087–1105.

SPEDDING, G. R. & HEDENSTROM, A. 2009 PIV-based investigation of animal flight. *Exp. Fluids* **46**, 749–763.

TRONCHIN, T., DAVID, L. & FARCY, A. 2013 Loads and pressure evaluation of the flow around a flapping wing. In *10th International Symposium on Particle Image Velocimetry–PIV13*. Delft, The Netherlands.

UNAL, M. F., LIN, J.-C. & ROCKWELL, D. 1997 Force prediciton by PIV imaging: a momentum-based approach. *J. Fluids Struct.* **11**, 965–971.

VAN OUDHEUSDEN, B. W. 2013 PIV-based pressure measurement. *Meas. Sci. Technol.* **24**, 032001.

VAN OUDHEUSDEN, B. W., SCARANO, F., ROOSENBOOM, E. W. M., CASIMIRI, E. W. F. & SOUVEREIN, L. J. 2007 Evalulation of integral forces and pressure fields from planar velocimetry data for incompressible and compressible flows. *Exp. Fluids* **43**, 153–162.

VILLEGAS, A. & DIEZ, F. J. 2014 On the quasi-instantaneous aerodynamic load and pressure field measurements on turbines by non-intrusive PIV. *Renew. Energy* **63**, 181–193.

WILLIAMSON, C. H. K. & GOVARDHAN, R. 2004 Vortex-induced vibrations. *Annu. Rev. Fluid Mech.* **36**, 413–455.

WU, J. C. 1981 Theory for aerodynamic force and moment in viscous flows. *AIAA J.* **19** (4), 432–441.